

All-electron Quasiparticle Self-consistent GW for Molecules and Periodic Systems within the Numerical Atomic Orbital Framework

Bohan Jia,^{1,2} Min-Ye Zhang,^{1,3,*} Ziqing Guan,^{1,2} Huanjing Gong,^{1,2} and Xinguo Ren^{1,†}

¹*Institute of Physics, Chinese Academy of Sciences, Beijing 100190, China*

²*School of Physical Sciences, University of Chinese Academy of Sciences, Beijing 100049, China*

³*The NOMAD Laboratory at the FHI Molecular Physics Department of the Max-Planck-Gesellschaft, Berlin 14195, Germany*

(Dated: March 3, 2026)

We report an all-electron implementation of the quasiparticle self-consistent GW (QSGW) method for molecules and periodic systems within the framework of numerical atomic orbitals (NAOs), as implemented in the LibRPA software package. We present systematic benchmark calculations on molecular systems, as well as a diverse set of periodic systems including typical semiconductors and wide-gap insulators. Our results demonstrate that the present NAO-based QSGW workflow yields molecular ionization potentials and quasiparticle band gaps for periodic solids that are consistent with established reference benchmarks, supporting the correctness of the implementation.

I. INTRODUCTION

In computational chemistry and condensed matter physics, accurately solving the quantum many-body problem from first principles remains a fundamental challenge. While Kohn-Sham (KS) density functional theory (DFT) [1, 2] is the most widely adopted approach, it suffers from well-known limitations of approximate exchange-correlation (XC) functionals, particularly in predicting excited-state properties and describing strongly correlated systems. For a large variety of molecules and materials, many-body perturbation theory within the GW approximation [3–14] offers a satisfactory approach for quantitatively describing single-particle excitations. Within GW , the many-body self-energy is given by the product of the Green’s function G and the screened Coulomb interaction W , which captures the dominant screening processes in a many-body system and yields physically meaningful quasiparticle energies.

Over the past four decades, the GW method has been developed into a versatile approach encompassing a variety of practical computational schemes, depending on whether and how self-consistency is incorporated. The simplest variant of GW is the so-called G^0W^0 scheme, where the Green’s function G^0 and screened Coulomb interaction W^0 are constructed from the outputs of a preceding mean-field calculation. G^0W^0 based on KS-DFT starting points with local or semilocal exchange-correlation functionals, such as the local density approximation (LDA) or generalized gradient approximations (GGAs) [9, 13, 15], has proven highly successful in predicting quantitatively accurate electronic band gaps for a large variety of materials.

However, as a one-shot perturbative scheme, G^0W^0 results inevitably exhibit a noticeable dependence on the starting point, i.e., the XC functional employed in the preceding mean-field calculation [16–20]. In particular,

for materials with complex electronic structures where LDA and GGAs perform poorly, it is often not *a priori* clear which starting point is appropriate. Furthermore, many applications require not only quasiparticle energies but also updated charge densities and wavefunctions beyond KS-DFT, which G^0W^0 cannot provide.

In principle, solving the set of GW equations in a fully self-consistent manner (the so-called sc GW scheme) is feasible [21–34]. In the fully self-consistent limit, sc GW is conserving in the sense of Baym and Kadanoff and removes the explicit starting-point dependence [35, 36]. However, sc GW is computationally demanding and, without vertex corrections, often overestimates band gaps for semiconductors and insulators [28, 37]. Moreover, neither G^0W^0 nor sc GW provides an updated single-particle Hamiltonian with explicit quasiparticle wavefunctions, which restricts their utility in theoretical analyses requiring orbital information, such as investigations of topological materials. These limitations motivate the development of an alternative approach that can deliver quasiparticle solutions while maintaining theoretical rigor. The quasiparticle self-consistent GW (QSGW) method, developed by Faleev, van Schilf-gaarde, and Kotani [38–40], fulfills these requirements.

The fundamental principle of QSGW is to approximate the dynamic self-energy $\Sigma(\omega)$ by a static, Hermitian XC potential V^{xc} . This potential is used to iteratively update a static mean-field Hamiltonian until self-consistency is reached, enabling the simultaneous optimization of quasiparticle energies and wavefunctions. Different prescriptions exist for constructing the static, Hermitian V^{xc} from $\Sigma(\omega)$, including the commonly used “Mode A”/“Mode B” constructions [39] and SRG-based approaches [41]. Moreover, QSGW can be systematically improved by incorporating vertex corrections (e.g., ladder diagrams in W) [42–46] and lattice-polarization effects on W [47]. In this work, we adopt the standard formulation proposed by the original authors [38–40]. The reliability and broad applicability of this approach have been extensively validated across a diverse range of materials, from conventional semiconductors to complex tran-

* minyez@iphy.ac.cn

† renxg@iphy.ac.cn

sition metal oxides [48, 49].

Naturally, the performance of the QSGW method is closely tied to the underlying numerical implementation. Over the years, QSGW has been implemented within various numerical frameworks, including linear muffin-tin orbitals (LMTO) [40], augmented-plane-wave based all-electron methods [49, 50], Gaussian-type orbitals (GTOs)[51], and more recently on graphics processing units (GPUs) [52]. Closely related self-consistent GW implementations in plane-wave projector augmented-wave (PAW) frameworks are also well established [28, 53].

In recent years, numerical atomic orbitals (NAOs) have emerged as a powerful basis-set framework for electronic structure calculations. NAOs offer several key advantages. First, the strict localization of NAO basis functions naturally facilitates the description of localized states—such as core electrons and strongly correlated d/f electrons—enabling all-electron calculations without the need for pseudopotentials. Second, the compactness of NAOs significantly reduces the dimensionality of the Hilbert space. Unlike plane-wave methods, which require thousands of basis functions and a large number of unoccupied states to converge the screened interaction, NAOs typically require only tens to hundreds of functions, thereby greatly alleviating the slow convergence with respect to the number of unoccupied states. Furthermore, when combined with the resolution of identity (RI) technique [54–57], two-electron integrals within the NAO framework can be efficiently decomposed, drastically reducing memory requirements and improving computational scaling. Benchmarks using established NAO codes, such as FHI-aims, demonstrate that the accuracy achieved on the GW100 test set [58] is comparable to that of plane-wave implementations, while the compactness of NAO basis sets and low-scaling formulations can offer favorable efficiency [57, 59, 60].

Despite the existence of molecular and periodic G^0W^0 implementations based on NAOs [59–61], an all-electron QSGW implementation within the NAO framework has not yet been reported. This gap has hindered the application of NAO-based methods to complex systems where self-consistency is essential, such as topological materials and strongly correlated oxides.

Developing such an implementation is therefore highly desirable, as it would combine the computational efficiency of NAOs with the rigorous quasiparticle framework of QSGW.

In this paper, we present an implementation of the QSGW method based on all-electron NAOs within the LibRPA software package, applicable to both molecules and periodic systems. We systematically benchmark the performance of our implementation for the vertical ionization potentials (IPs) of small molecules from the GW100 test set, as well as the band gaps of a diverse range of semiconductors and insulators. Furthermore, we present a detailed comparison with the G^0W^0 method and other QSGW implementations to comprehensively evaluate the accuracy and reliability of our approach.

This paper is organized as follows. In Sec. II, we outline the theoretical framework, detailing the QSGW formalism and its implementation using the NAO-based real-space formalism combined with the localized resolution of identity (LRI) technique. Sec. III discusses specific implementation details in LibRPA, including the self-consistency workflow, convergence behavior, and an analysis of the basis dependence in the analytic continuation process. Sec. IV presents benchmark results for molecular systems (Sec. IV A) and periodic solids (Sec. IV B), comparing our results with standard DFT, G^0W^0 , and other QSGW implementations. Finally, we summarize our findings and provide an outlook in Sec. V.

II. THEORETICAL FRAMEWORK

This section outlines the theoretical foundations of the QSGW method. We begin with a review of the GW approximation and the one-shot G^0W^0 approach, followed by a detailed formulation of the QSGW scheme. We then present the NAO-based formalism combined with the localized resolution of identity (LRI) technique, which forms the algorithmic basis of our implementation.

A. The GW approximation and the G^0W^0 scheme

In quantum many-body theory, the central quantity is the single-particle Green’s function G , which describes the propagation of an electron or hole in an interacting many-body system.

The interacting Green’s function satisfies the Dyson equation, which relates it to the non-interacting Green’s function G^0 via the self-energy Σ :

$$G(\mathbf{r}, \mathbf{r}', \omega) = G^0(\mathbf{r}, \mathbf{r}', \omega) + \int d\mathbf{r}_1 d\mathbf{r}_2 G^0(\mathbf{r}, \mathbf{r}_1, \omega) \Sigma(\mathbf{r}_1, \mathbf{r}_2, \omega) G(\mathbf{r}_2, \mathbf{r}', \omega). \quad (1)$$

The self-energy Σ accounts for all XC effects beyond the mean-field Hartree level and needs to be approximated in practical calculations. The poles of G yield the quasiparticle excitations which, compared to the bare particles (electrons), possess renormalized properties such as modified effective masses and finite lifetimes.

The accuracy of the calculated Green’s function depends critically on the approximation chosen for the self-energy. In this context, the GW approximation (GWA) corresponds to a specific choice of self-energy diagrams, where Σ is given by the product of G and the dynamically screened Coulomb interaction W . In the standard one-shot G^0W^0 scheme, the self-energy is evaluated non-self-consistently using an initial G^0 :

$$\Sigma(\mathbf{r}, \mathbf{r}', \omega) = \frac{i}{2\pi} \int d\omega' G^0(\mathbf{r}, \mathbf{r}', \omega + \omega') W^0(\mathbf{r}, \mathbf{r}', \omega') \quad (2)$$

where W^0 is the screened Coulomb interaction calculated typically within the random phase approximation (RPA).

Concretely, W^0 can be expressed as

$$W^0(\mathbf{r}, \mathbf{r}', \omega) = \int d\mathbf{r}_1 \varepsilon^{-1}(\mathbf{r}, \mathbf{r}_1, \omega) v(\mathbf{r}_1, \mathbf{r}'). \quad (3)$$

where ε^{-1} is the inverse of the dielectric function ε , which describes the screening process and can be computed as

$$\varepsilon(\mathbf{r}, \mathbf{r}', \omega) = \delta(\mathbf{r} - \mathbf{r}') - \int d\mathbf{r}_1 v(\mathbf{r}, \mathbf{r}_1) \chi^0(\mathbf{r}_1, \mathbf{r}', \omega). \quad (4)$$

Here, $v(\mathbf{r}, \mathbf{r}') = 1/|\mathbf{r} - \mathbf{r}'|$ is the bare Coulomb interaction and χ^0 is the irreducible polarizability. Under the RPA, χ^0 equals the non-interacting density response function that is given by

$$\chi^0(\mathbf{r}, \mathbf{r}', \omega) = -\frac{i}{2\pi} \int d\omega' G^0(\mathbf{r}, \mathbf{r}', \omega + \omega') G^0(\mathbf{r}', \mathbf{r}, \omega'). \quad (5)$$

As is evident from the above equations, in the G^0W^0 approach, the calculation relies entirely on the non-interacting Green's function G^0 , which is typically constructed from a preceding DFT calculation:

$$G^0(\mathbf{r}, \mathbf{r}', \omega) = \sum_p (1 - f_p) \frac{\psi_p(\mathbf{r}) \psi_p^*(\mathbf{r}')}{\omega + \epsilon_F - \epsilon_p + i\eta} + \sum_p f_p \frac{\psi_p(\mathbf{r}) \psi_p^*(\mathbf{r}')}{\omega + \epsilon_F - \epsilon_p - i\eta} \quad (6)$$

where $\psi_p(\mathbf{r})$ and ϵ_p are the KS orbitals and orbital energies, respectively, f_p is the occupation number, ϵ_F is the Fermi energy (chemical potential), and η is a positive infinitesimal.

Within the G^0W^0 approach, the quasiparticle excitation energies are obtained by solving the quasiparticle equation

$$\epsilon_p^{\text{QP}} = \epsilon_p + \text{Re}\langle \psi_p | \Sigma(\epsilon_p^{\text{QP}}) - V^{\text{xc}} | \psi_p \rangle, \quad (7)$$

where the self-energy depends on the quasiparticle energy itself. This nonlinear equation is solved self-consistently for each state, typically by root-finding algorithms. Importantly, in G^0W^0 , the Green's function G^0 and screened interaction W^0 are fixed from the initial DFT calculation and are not updated during this process—hence the term “one-shot” GW . Only the diagonal elements of the self-energy matrix are required.

However, as discussed in Sec. I, G^0W^0 does not provide updated charge densities or quasiparticle wavefunctions beyond the initial KS calculation. The QSGW method, described in the following subsection, addresses this limitation by providing a self-consistent framework that simultaneously updates both quasiparticle energies and wavefunctions.

B. The QSGW scheme

The QSGW scheme aims to find an effective static and Hermitian Hamiltonian that best approximates the effective dynamical GW Hamiltonian. In general, we can write such a Hamiltonian as

$$H^{\text{QSGW}} = -\frac{1}{2} \nabla^2 + V^{\text{ext}}(\mathbf{r}) + V^{\text{H}}(\mathbf{r}) + V^{\text{xc}}, \quad (8)$$

where the first three terms – the kinetic energy operator, the external potential operator, and the Hartree potential operator – are the same as in the usual KS Hamiltonian, whereas the final term, the XC potential operator V^{xc} , represents a static, Hermitian approximation to the dynamic GW self-energy $\Sigma^{\text{GW}}(\omega)$. In practice, there are different choices of the actual procedure to construct the XC potential for QSGW, with the two most prominent schemes being referred to as “Mode A” and “Mode B” [39]. Specifically, in “Mode A”, the XC potential is defined as:

$$V^{\text{xc}} = \frac{1}{2} \sum_{pp'} |\psi_p\rangle \{ \text{Re}[\Sigma^{\text{GW}}(\epsilon_p)]_{pp'} + \text{Re}[\Sigma^{\text{GW}}(\epsilon_{p'})]_{pp'} \} \langle \psi_{p'} |, \quad (9)$$

whereas in “Mode B”, it is defined as:

$$V^{\text{xc}} = \sum_p |\psi_p\rangle \text{Re}[\Sigma^{\text{GW}}(\epsilon_p)]_{pp} \langle \psi_p | + \sum_{p \neq p'} |\psi_p\rangle \text{Re}[\Sigma^{\text{GW}}(\epsilon_F)]_{pp'} \langle \psi_{p'} |. \quad (10)$$

Here ϵ_p is the p -th eigenvalue of the Hamiltonian H^{QSGW} , ϵ_F is the Fermi energy, and “Re” denotes the Hermitian part of the self-energy matrix, i.e., $\text{Re}[A]_{pp'} \equiv (A_{pp'} + A_{p'p}^*)/2$. Formally, the construction in “Mode A” can also be derived by minimizing the length of the gradient of the Klein total energy functional over non-interacting Green's functions (given by $(\omega - H^{\text{QSGW}})^{-1}$), as demonstrated by Ismail-Beigi [62].

In a practical self-consistent QSGW calculation, the following steps need to be executed iteratively:

1. Start with an initial guess for the effective potential V^{xc} , usually taken from a preceding DFT calculation.
2. Construct the effective Hamiltonian H^{QSGW} using the current V^{xc} and solve the eigenvalue problem to obtain the QSGW orbitals $\psi_p(\mathbf{r})$ and eigenvalues ϵ_p .
3. Build the non-interacting Green's function G^0 from the QSGW orbitals and eigenvalues.
4. Calculate the self-energy $\Sigma(\mathbf{r}, \mathbf{r}', \omega)$ using the GW approximation based on G^0 as described in Eqs. (2)–(6).

5. Update the effective potential V^{xc} using the chosen QSGW mode (A or B) to obtain a new static and Hermitian approximation of the self-energy.
6. Check for convergence. If the change in the quasi-particle energies is below a predefined threshold, the calculation is considered converged. Otherwise, return to step 2.

The above-outlined QSGW scheme has been implemented in the LibRPA package [61, 63]. LibRPA was originally developed for the RPA correlation energy [63] and one-shot G^0W^0 calculations [61]. LibRPA is interfaced with FHI-aims to acquire necessary inputs from DFT calculations. We use the NAO-based real-space formalism combined with the localized resolution of identity (LRI) technique to construct the XC potential operator of QSGW efficiently, which will be detailed in the next subsection.

C. NAO-based formalism for QSGW

To implement the QSGW formalism efficiently within the NAO framework, we employ a space-time approach [60, 61] combined with the LRI technique [64]. This approach facilitates the computation of the full GW self-energy matrix required by the QSGW scheme. Furthermore, the use of NAO basis functions and the LRI technique gives rise to significant sparsity in the LRI expansion coefficients. Exploiting this sparsity leads to an $\mathcal{O}(N^2)$ -scaling algorithm for constructing the GW self-energy, compared to the $\mathcal{O}(N^4)$ scaling in the conventional approach. A detailed description of the underlying G^0W^0 implementation has been provided in a separate work [61]. Here, we only summarize the key steps and equations specific to the QSGW implementation.

1. NAO basis set representation

First, the single-particle orbitals (KS orbitals in the initial iteration, or the QSGW orbitals in subsequent iterations) are expanded in a basis of numerical atomic orbitals (NAOs):

$$\psi_{p\mathbf{k}}(\mathbf{r}) = \sum_i c_{p\mathbf{k}}^i \varphi_{i\mathbf{k}}(\mathbf{r}) \quad (11)$$

Here, $c_{p\mathbf{k}}^i$ are the expansion coefficients for the p -th state at Bloch wavevector \mathbf{k} in terms of the NAO basis. The Bloch sums of NAOs are defined as:

$$\varphi_{i\mathbf{k}}(\mathbf{r}) = \frac{1}{\sqrt{N_{\mathbf{k}}}} \sum_{\mathbf{R}} e^{i\mathbf{k}\cdot\mathbf{R}} \varphi_{i\mathbf{R}}(\mathbf{r}), \quad (12)$$

with each localized NAO taking the form:

$$\varphi_{i\mathbf{R}}(\mathbf{r}) = u_{\kappa l}(|\mathbf{r} - \mathbf{t}_I - \mathbf{R}|) S_{lm}(\mathbf{r} - \widehat{\mathbf{t}_I - \mathbf{R}}). \quad (13)$$

Here, $u_{\kappa l}$ denotes the radial part of the NAO and S_{lm} corresponds to the real spherical harmonics. The composite index $i = \{I, \kappa, l, m\}$ specifies the atomic center I , the radial function index κ , and the angular quantum numbers (l, m) . Furthermore, \mathbf{R} is the lattice translation vector, and \mathbf{t}_I represents the position of atom I within the unit cell.

2. Localized resolution of identity technique

For QSGW, similar to our implementation of RPA [63, 65] and G^0W^0 [60, 61], we employ an auxiliary basis set to represent the two-electron quantities and LRI to decompose the four-index tensors into three- and two-index ones. In this approach, a key step is to expand the products of NAOs in terms of auxiliary basis functions (ABFs):

$$\begin{aligned} \varphi_{i\mathbf{R}}(\mathbf{r})\varphi_{j\mathbf{R}'}(\mathbf{r}) &\approx \sum_{\mu \in I} C_{i(\mathbf{R}),j(\mathbf{R}')}^{\mu(\mathbf{R})} P_{\mu\mathbf{R}}(\mathbf{r}) \\ &+ \sum_{\mu \in J} C_{i(\mathbf{R}),j(\mathbf{R}')}^{\mu(\mathbf{R}')} P_{\mu\mathbf{R}'}(\mathbf{r}), \end{aligned} \quad (14)$$

where $P_{\mu\mathbf{R}}(\mathbf{r})$ denotes the ABFs which are required to be centered on atoms I or J , on which the two NAOs are located. In Eq. 14, $C_{i(\mathbf{R}),j(\mathbf{R}')}^{\mu(\mathbf{R})}$ are the LRI expansion coefficients, and the lattice vector \mathbf{R} in parentheses specifies the unit cell where the NAO i or ABF μ is localized in a periodic system.

Now, by substituting this expansion into the four-orbital electron repulsion integrals, these computationally expensive integrals are decomposed into three-index tensors (involving two NAOs and one ABF) and two-index matrices (involving two ABFs). This decomposition constitutes the foundation for the efficient evaluation of self-energy terms, as explicitly demonstrated later in the construction of the correlation self-energy [see Eq. (23)].

3. Space-time formalism of QSGW with NAO and LRI

The non-interacting Green's function in real space and imaginary time is expressed in the NAO basis as:

$$G^0(\mathbf{r}, \mathbf{r}', i\tau) = \sum_{ij} \sum_{\mathbf{R}, \mathbf{R}'} \varphi_{i\mathbf{R}}(\mathbf{r}) G_{ij}^0(\mathbf{R}' - \mathbf{R}, i\tau) \varphi_{j\mathbf{R}'}(\mathbf{r}'), \quad (15)$$

with the matrix elements given by

$$G_{ij}^0(\mathbf{R}, i\tau) = \frac{1}{N_{\mathbf{k}}} \sum_{p\mathbf{k}} e^{-i\mathbf{k}\cdot\mathbf{R}} c_{p\mathbf{k}}^i c_{p\mathbf{k}}^{j*} \Xi_{p\mathbf{k}}(\tau), \quad (16)$$

where

$$\Xi_{p\mathbf{k}}(\tau) = e^{-(\epsilon_{p\mathbf{k}} - \epsilon_F)\tau} [\theta(\tau)(1 - f_{p\mathbf{k}}) - \theta(-\tau)f_{p\mathbf{k}}]. \quad (17)$$

Here $\theta(\tau)$ is the Heaviside step function, $f_{p\mathbf{k}}$ is the occupation number, and ϵ_F is the Fermi energy (chemical potential). For the sake of simplicity, only the spin-degenerate case with integer orbital occupations is considered. The extension to the spin polarized case is straightforward.

Using LRI, the irreducible polarizability in real space and imaginary time is expanded in terms of ABFs,

$$\chi^0(\mathbf{r}, \mathbf{r}', i\tau) = \sum_{\mu\nu} \sum_{\mathbf{R}, \mathbf{R}'} P_{\mu\mathbf{R}}(\mathbf{r}) \chi_{\mu\nu}^0(\mathbf{R}' - \mathbf{R}, i\tau) P_{\nu\mathbf{R}'}(\mathbf{r}'), \quad (18)$$

where the polarizability matrix is computed as (see Refs. [63, 65]):

$$\begin{aligned} \chi_{\mu\nu}^0(\mathbf{R}, i\tau) &= -i \sum_{ijkl} \sum_{\mathbf{R}_1, \mathbf{R}_2} C_{i(\mathbf{0}),k(\mathbf{R}_1)}^{\mu(\mathbf{0})} C_{j(\mathbf{R}),l(\mathbf{R}+\mathbf{R}_2)}^{\nu(\mathbf{R})} \\ &\times \left[G_{ij}^0(\mathbf{R}, i\tau) G_{lk}^0(\mathbf{R}_1 - \mathbf{R} - \mathbf{R}_2, -i\tau) \right. \\ &\left. + G_{ij}^0(\mathbf{R}, -i\tau)^* G_{lk}^0(\mathbf{R}_1 - \mathbf{R} - \mathbf{R}_2, i\tau)^* \right]. \quad (19) \end{aligned}$$

Here, $C_{i(\mathbf{0}),k(\mathbf{R}')}^{\mu(\mathbf{0})}$ are the LRI expansion coefficients introduced in Eq. 14. In practical calculations, $C_{i(\mathbf{0}),k(\mathbf{R}')}^{\mu(\mathbf{0})}$ are provided by FHI-aims, interfaced with LibRPA.

The next key quantity is the screened Coulomb matrix represented within the ABF basis, which is computed as:

$$W_{\mu\nu}^0(\mathbf{q}, i\omega) = \sum_{\mu'\nu'} V_{\mu\mu'}^{1/2} [\tilde{\epsilon}^{-1}(\mathbf{q}, i\omega)]_{\mu'\nu'} V_{\nu'\nu}^{1/2}, \quad (20)$$

where $V^{1/2}$ is the square root of the bare Coulomb matrix V , and $\epsilon^{-1}(\mathbf{q}, i\omega)$ is the inverse of the symmetrized dielectric function ϵ , given by

$$\tilde{\epsilon}_{\mu\nu}(\mathbf{q}, i\omega) = \delta_{\mu\nu} - \sum_{\mu'\nu'} V_{\mu\mu'}^{1/2}(\mathbf{q}) \chi_{\mu'\nu'}^0(\mathbf{q}, i\omega) V_{\nu'\nu}^{1/2}(\mathbf{q}). \quad (21)$$

Here \mathbf{q} denotes the momentum transfer (wave vector of the dielectric response), equivalent to $\mathbf{k} - \mathbf{k}'$. For a uniform \mathbf{k} mesh, the \mathbf{q} mesh is the same as the \mathbf{k} one, but they can differ in general cases.

To calculate the dielectric function using Eq. 21, the irreducible polarization function χ^0 needs to be Fourier transformed from the imaginary time axis to the imaginary frequency axis. This can be efficiently done using MiniMax time/frequency grids [66, 67].

Now, we can calculate the correlation part of the self-energy in the NAO basis as follows:

$$\Sigma_{pp'}^c(\mathbf{k}, i\tau) = \sum_{ij} c_{p\mathbf{k}}^{i*} c_{p'\mathbf{k}}^j \sum_{\mathbf{R}} e^{i\mathbf{k}\cdot\mathbf{R}} \Sigma_{ij}^c(\mathbf{R}, i\tau). \quad (22)$$

Here, the correlation matrix elements $\Sigma_{ij}^c(\mathbf{R}, i\tau)$ can be expressed in terms of LRI coefficients, the screened

Coulomb interaction $W_{\mu\nu}^c(\mathbf{R}, i\tau)$, and the Green's function as:

$$\begin{aligned} \Sigma_{ij}^c(\mathbf{R}, i\tau) &= - \sum_{k\mathbf{R}_1} \sum_{l\mathbf{R}_2} G_{kl}^0(\mathbf{R}_2 - \mathbf{R}_1, i\tau) \\ &\times \left[\sum_{\mu \in I} \sum_{\nu \in J} C_{i(\mathbf{0}),k(\mathbf{R}_1)}^{\mu(\mathbf{0})} W_{\mu\nu}^c(\mathbf{R}, i\tau) C_{j(\mathbf{R}),l(\mathbf{R}_2)}^{\nu(\mathbf{R})} \right. \\ &+ \sum_{\mu \in K} \sum_{\nu \in J} C_{i(\mathbf{0}),k(\mathbf{R}_1)}^{\mu(\mathbf{R}_1)} W_{\mu\nu}^c(\mathbf{R} - \mathbf{R}_1, i\tau) C_{j(\mathbf{R}),l(\mathbf{R}_2)}^{\nu(\mathbf{R})} \\ &+ \sum_{\mu \in I} \sum_{\nu \in L} C_{i(\mathbf{0}),k(\mathbf{R}_1)}^{\mu(\mathbf{0})} W_{\mu\nu}^c(\mathbf{R}_2, i\tau) C_{j(\mathbf{R}),l(\mathbf{R}_2)}^{\nu(\mathbf{R}_2)} \\ &\left. + \sum_{\mu \in K} \sum_{\nu \in L} C_{i(\mathbf{0}),k(\mathbf{R}_1)}^{\mu(\mathbf{R}_1)} W_{\mu\nu}^c(\mathbf{R}_2 - \mathbf{R}_1, i\tau) C_{j(\mathbf{R}),l(\mathbf{R}_2)}^{\nu(\mathbf{R}_2)} \right]. \quad (23) \end{aligned}$$

Here, the GW self-energy is decomposed as $\Sigma = \Sigma^x + \Sigma^c$. The correlation part uses $W_{\mu\nu}^c \equiv W_{\mu\nu}^0 - V_{\mu\nu}$, whereas the exchange part is obtained from the same LRI machinery by using the bare Coulomb interaction $V_{\mu\nu}$ and is therefore omitted here; see Ref. [61] for implementation details.

The screened Coulomb matrix in real space and imaginary time $W_{\mu\nu}^c(\mathbf{R}, i\tau)$ is obtained from its counterpart in \mathbf{q} space and imaginary frequency via Fourier transform. Further details of our implementation are presented in Ref. [61].

Thus, we have constructed all the necessary components to compute the dynamic self-energy $\Sigma(\omega)$ within the NAO and LRI framework using the space-time formalism. To obtain the self-energy on the real frequency axis, we perform an analytic continuation from imaginary frequencies using the Padé approximant method [68].

The final step in our QSGW implementation is the construction of the static, Hermitian XC potential matrix V^{xc} that approximates the dynamical self-energy $\Sigma(\omega)$. The self-energy matrix elements in the eigenbasis are computed as:

$$\Sigma_{pp'}(\mathbf{k}, \omega) = \langle \psi_{p\mathbf{k}} | \Sigma(\omega) | \psi_{p'\mathbf{k}} \rangle = \sum_{ij} c_{p\mathbf{k}}^{i*} c_{p'\mathbf{k}}^j \Sigma_{ij}(\mathbf{k}, \omega), \quad (24)$$

where $\Sigma_{ij}(\mathbf{k}, \omega)$ are the matrix elements in the NAO basis and $\Sigma_{pp'}(\mathbf{k}, \omega)$ are those in the eigenbasis of the QSGW Hamiltonian.

Subsequently, the QSGW XC potential V^{xc} is constructed according to either ‘‘Mode A’’ or ‘‘Mode B’’, as defined in Eqs. (9) and (10).

The combination of NAOs, LRI, and the space-time formalism provides an efficient framework for QSGW calculations, maintaining accuracy while keeping the computational cost tractable for large extended systems.

III. IMPLEMENTATION DETAILS

A. QSGW in LibRPA

Our QSGW implementation is built upon the existing space-time G^0W^0 framework within the LibRPA software package [61]. Here, we focus on the specific extensions required for the self-consistent scheme, as illustrated in Fig. 1.

First, a standard KS-DFT calculation is performed to obtain an initial Kohn-Sham Hamiltonian $H^{\text{KS,DFT}}$, along with the corresponding orbitals and eigenvalues. We employ FHI-aims as the DFT engine to generate the initial input for LibRPA. At the beginning of the QSGW iteration, the non-XC part of the Hamiltonian is extracted from the KS-DFT calculation and remains fixed throughout the QSGW iterations. Namely, the DFT XC potential is first subtracted from the KS Hamiltonian:

$$H^{\text{non-xc}} = -\frac{1}{2}\nabla^2 + V^{\text{ext}}(\mathbf{r}) + V^{\text{H}}(\mathbf{r}) = H^{\text{KS,DFT}} - V^{\text{xc,DFT}}, \quad (25)$$

and the resultant $H^{\text{non-xc}}$ will be combined with the V^{xc} matrix derived from the GW self-energy to build the QSGW Hamiltonian.

Subsequently, the QSGW iteration proceeds analogously to a standard G^0W^0 calculation in LibRPA until the self-energy on the imaginary frequency axis, $\Sigma_{ij}(\mathbf{k}, i\omega)$, is obtained.

A Padé approximation is then employed to perform the analytic continuation from the imaginary frequency axis to the real frequency axis, yielding the self-energy at real frequencies, $\Sigma_{ij}(\mathbf{k}, \omega_{\text{real}})$. A detailed discussion on the stability of this analytic continuation is provided in Sec. III B.

Once the dynamic self-energy is obtained, the static and Hermitian XC potential V^{xc} is constructed according to either ‘‘Mode A’’ or ‘‘Mode B’’, as defined in Eqs. (9) and (10).

Finally, the updated orbitals and eigenvalues are fed back into LibRPA to execute the next QSGW iteration. This process is repeated until the quasiparticle energies are converged within a predefined threshold, typically set to 10^{-3} eV in our calculations. The n -th QSGW Hamiltonian can thus be expressed as:

$$H^{\text{QSGW},n}(\mathbf{k}) = H^{\text{non-xc}}(\mathbf{k}) + V^{\text{xc,QSGW},n}(\mathbf{k}). \quad (26)$$

To improve the stability of the self-consistency cycle for molecular systems, we employ Pulay’s DIIS mixing method [69] when updating the QSGW Hamiltonian. For periodic systems, the iterations are generally stable in our benchmarks and converge without DIIS mixing. Our QSGW implementation typically requires 6–10 iterations to achieve convergence of eigenvalues within 10^{-3} eV for periodic systems, whereas molecular systems may still require tens to hundreds of iterations. Upon convergence, the final quasiparticle energies and orbitals are utilized

to compute various electronic properties, such as band structures and topological invariants.

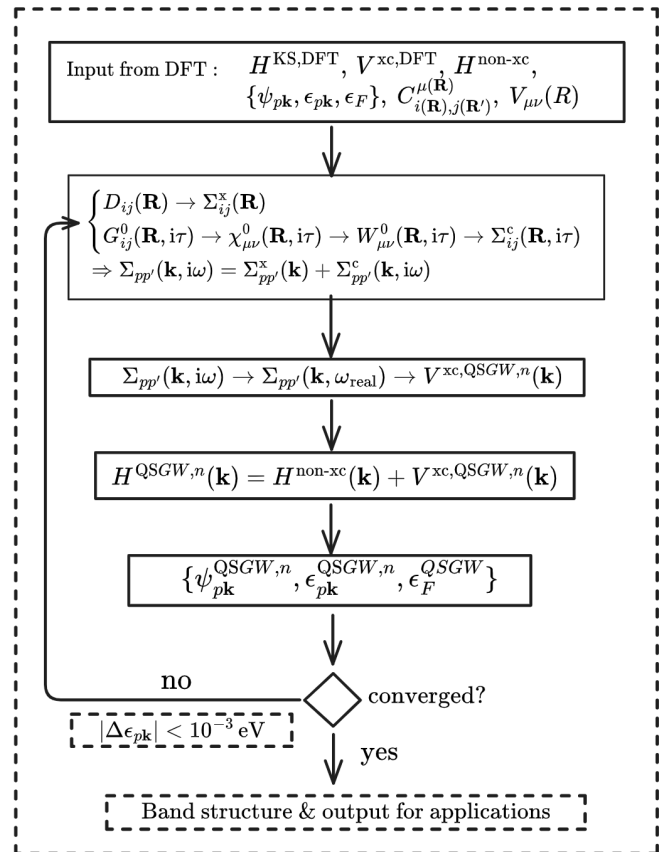


FIG. 1. Workflow of the QSGW calculation, starting from a KS-DFT calculation and converging to self-consistency using the LibRPA software. Indices i, j label NAO basis functions (composite index $i = \{I, \kappa, l, m\}$ with magnetic quantum number m in S_{lm}); p, p' label single-particle eigenstates $\psi_{p\mathbf{k}}$; \mathbf{k} is the Bloch wave vector; \mathbf{q} is the momentum transfer used in $W^0_{\mu\nu}(\mathbf{q}, i\omega)$; I, J represent atom indices; and n is the iteration number.

B. Analytic continuation of self-energy

In this work, we employ the Padé approximation to perform the analytic continuation of the self-energy from the imaginary frequency axis to the real frequency axis. As previously reported [70], the Padé analytic continuation in QSGW is significantly more sensitive to numerical noise compared to standard G^0W^0 calculations, which can affect the stability and accuracy of the results. This sensitivity arises from the fact that standard G^0W^0 calculations require only the diagonal elements of the self-energy matrix for quasiparticle energy calculations, whereas in QSGW, the full self-energy matrix is needed to construct the static XC potential V^{xc} . The off-diagonal elements of the self-energy matrix are usually small in magnitude, making them particularly susceptible to numerical noise introduced during the analytic

continuation process.

Theoretically, in the absence of numerical noise, the analytic continuation of $\Sigma(i\omega)$ should yield identical results regardless of the basis representation (e.g., the initial KS basis or the updated QSGW eigenbasis). In this section, “basis” refers to this representation choice for Σ and its analytic continuation, and should not be confused with the underlying NAO basis settings (e.g., `intermediate_gw`, `really_tight`). However, numerical noise inevitably introduces a basis representation dependence. To evaluate the impact of this dependence, particularly regarding different QSGW construction schemes, we performed calculations on Si and MgO using both “Mode A” and “Mode B”. We compared the results obtained in two different basis representations: the initial KS basis from DFT and the updated QSGW eigenbasis (obtained by diagonalizing the QSGW Hamiltonian from the previous iteration, as defined in Eq. (26)).

As illustrated in Fig. 2, “Mode A” exhibits significant basis representation dependence for both Si and MgO. Notably, when the iteration number exceeds 3, the band gaps calculated using “Mode A” in different basis representations begin to diverge significantly. In contrast, “Mode B” demonstrates much better consistency between different basis representations, implying that the analytic continuation in “Mode B” is far less sensitive to numerical noise. Specifically, after 5 iterations, the difference in band gaps calculated using the two different basis representations for “Mode B” converges to within 10^{-2} eV for both materials. Furthermore, “Mode B” exhibits faster convergence rates compared to “Mode A”. Consequently, while “Mode A” may require more robust analytic continuation techniques—such as the maximum entropy method or stochastic optimization—to mitigate noise, “Mode B” proves to be numerically stable within our current framework.

Based on these tests for Si and MgO, we employ “Mode B” and perform analytic continuation in the initial KS basis for all benchmark calculations reported below.

However, we note that even “Mode B” exhibits a small but non-negligible basis representation dependence, as evidenced in Fig. 2. For Si, the band gaps converged in the KS basis and the updated QSGW eigenbasis differ by approximately 0.03 eV after 8 iterations (1.337 eV vs. 1.306 eV). A similar behavior is observed for MgO, with a difference of about 0.03 eV between the two basis representations (9.140 eV vs. 9.109 eV). We treat this residual spread as an estimate of the numerical uncertainty associated with the analytic-continuation protocol used here.

C. Convergence Behavior

To ensure the reliability and consistency of the QSGW results, we now proceed to discuss several key numerical parameters: the \mathbf{k} -point mesh, frequency grid, and basis settings.

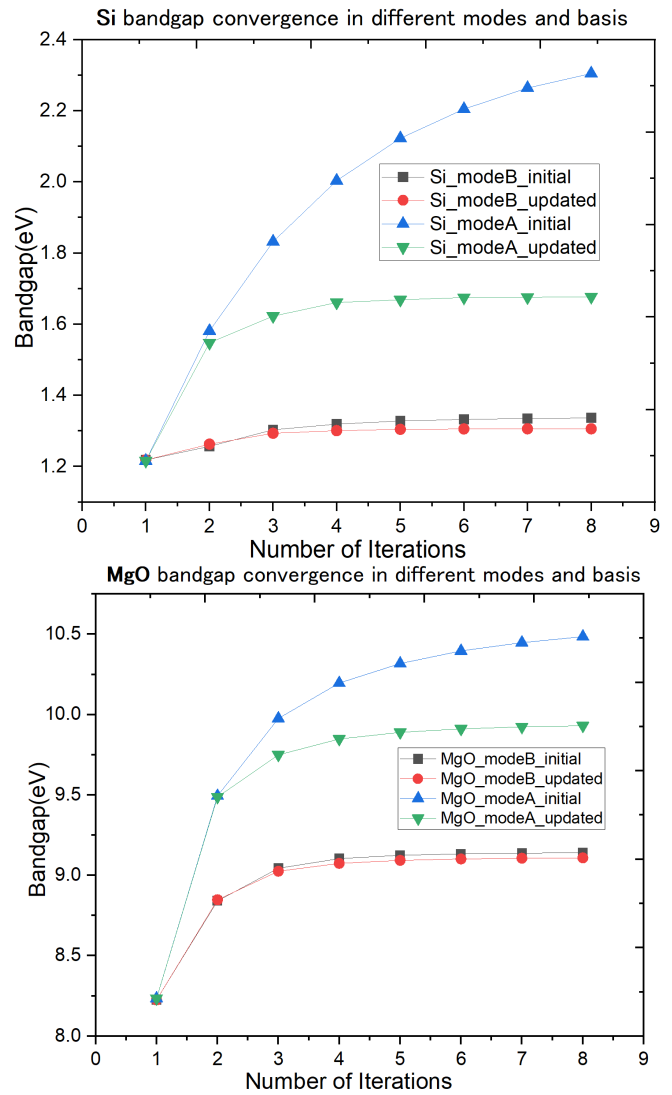


FIG. 2. Basis representation dependence tests of analytic continuation in QSGW for “Mode A” and “Mode B” for Si (top) and MgO (bottom). The Si calculations employed a $6 \times 6 \times 6$ \mathbf{k} -point mesh, while MgO employed an $8 \times 8 \times 8$ mesh. Both used a frequency grid of 16 points and the `intermediate_gw` basis sets. In the figure, “initial” denotes analytic continuation performed in the initial KS-DFT eigenbasis, while “updated” denotes analytic continuation performed in the updated QSGW eigenbasis from the previous iteration.

1. \mathbf{k} -point and frequency grid convergence

First, we test the \mathbf{k} convergence of the Si QSGW band gap with respect to Brillouin-zone sampling using uniform $n \times n \times n$ \mathbf{k} -point meshes ($n = 6-10$), as shown in Fig. 3. Taking the $10 \times 10 \times 10$ mesh as the reference, the residual QSGW band-gap difference decreases from 32 meV at $6 \times 6 \times 6$ to 6.5 meV at $9 \times 9 \times 9$ (with $E_g^{\text{QSGW}} = 1.3621$ eV at $9 \times 9 \times 9$ and $E_g^{\text{QSGW}} = 1.3686$ eV at $10 \times 10 \times 10$, i.e., a last-step change of 6.46 meV); at the adopted $8 \times 8 \times 8$ mesh the residual relative to $10 \times 10 \times 10$ is 12.5 meV, but this level of \mathbf{k} -point convergence is still

not fully satisfactory.

In the present implementation, a likely reason for this residual k -point sensitivity is that the head correction term (i.e., the Γ -point correction to the dielectric matrix; see Ref. [61]) is updated only in the first QSGW iteration and is kept fixed in subsequent iterations. For Si at the adopted $8 \times 8 \times 8$ mesh, we estimate the associated residual uncertainty in E_g to be on the order of 10–15 meV under the present protocol. We are continuing to improve this aspect by updating the treatment of the head correction term at each iteration.

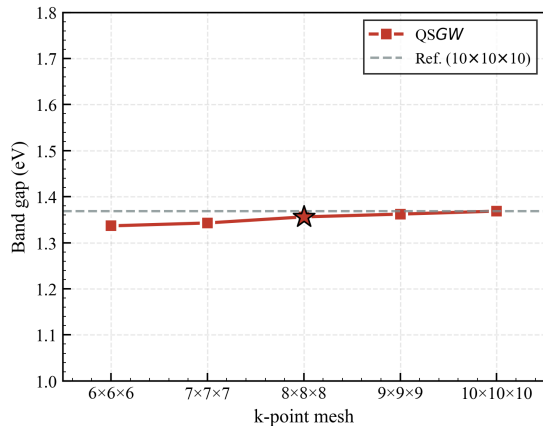


FIG. 3. k -point convergence of the Si QSGW band gap with respect to uniform $n \times n \times n$ k -point meshes ($n = 6$ – 10) using the `intermediate_gw` basis sets. The $10 \times 10 \times 10$ mesh is taken as the reference.

Regarding the frequency grid, we tested the convergence of the QSGW band gap with respect to the number of imaginary frequency points used in the self-energy calculation. Figure 4 shows the frequency grid convergence for Si using an $8 \times 8 \times 8$ k -point mesh and the `intermediate_gw` basis sets.

The results demonstrate that the QSGW band gap converges rapidly with respect to the frequency grid. Between 16 and 28 frequency points, the band gap varies by only 2.6 meV (from 1.356 eV to 1.354 eV), indicating that 16 frequency points are sufficient to achieve convergence within 3 meV. We note that the calculation with 32 frequency points yields a slightly higher band gap (1.357 eV), but the difference remains at the meV level. Based on these tests, we adopt 16 frequency points for the periodic systems in this work as a practical choice that reduces the computational cost while maintaining excellent accuracy. For the molecular benchmarks reported below, we employ 32 frequency points, since the additional cost is modest compared to periodic calculations and provides a conservative numerical setting.

2. Basis sets

For the benchmark calculations presented in this work, we adopt different basis sets for periodic solids

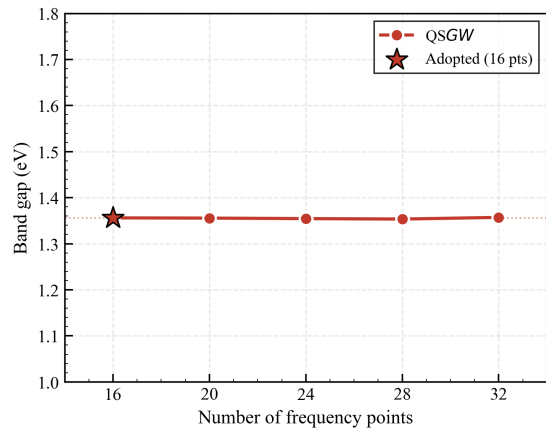


FIG. 4. Frequency grid convergence of the Si QSGW band gap using an $8 \times 8 \times 8$ k -point mesh and the `intermediate_gw` basis sets (see Sec. III C 2). The calculation with 16 frequency points (highlighted with a red star) is adopted for the periodic systems in this work. The band gap varies by only 2.6 meV between 16 and 28 frequency points, confirming adequate convergence.

and molecules. For periodic systems, we employ the `intermediate_gw` setting, which offers a practical compromise between accuracy and computational cost for the present test set. For molecular systems, we use the `really_tight` setting, i.e., the same orbital NAO basis as the `tight` basis sets but with more stringent numerical settings.

Here, `intermediate_gw` and `really_tight` denote the predefined FHI-aims `species_defaults` setting (defaults.2020), which explicitly specify (i) the orbital NAO basis (minimal basis plus additional confined radial functions, organized in tiers) and (ii) the associated numerical settings (integration grids and Hartree-potential accuracy) for each chemical element. In the defaults.2020 hierarchy, `intermediate` setting retains most numerical settings from `tight` but employs a more economical orbital basis, whereas `tight` setting corresponds to tier-based NAO orbital lists (e.g., "tier 2" for H–Ne and "tier 1" for most heavier elements), and `really_tight` setting keeps the same orbital basis as `tight` setting but uses strongly overconverged numerical parameters (including `basis_dep_cutoff=0`).[71]

In the corresponding RI-based GW workflow, the auxiliary basis refers to the atom-centered auxiliary basis functions used to expand products of orbital basis functions in the Coulomb-operator representation.

For periodic GW calculations, the corresponding `intermediate_gw` setting is identical to the standard `intermediate` setting except that it augments the ABFs used in the LRI (RI-LVL) representation of the Coulomb operator by adding extra `for_aux` functions (specifically, `for_aux hydro 4 f 0.0`); these `for_aux` functions are used only to generate the auxiliary basis and do not enter the KS orbital basis.[71, 72]

Both settings correspond to predefined FHI-aims NAO

Molecule	Exp. (IP)	QSGW (this work) (IP)	QSGW (ADF STO extra) (IP)	QSGW (TM def2-TZVPP) (IP)
Ag ₂	7.66	7.42	7.15	—
AlF ₃	15.45*	16.06	15.72	15.69
As ₂	10.00*	9.78	9.66	9.62
AsH ₃	10.58*	10.63	10.70	10.50
BF	11.00	11.22	11.20	11.13
BH ₃	12.03	13.65	13.61	13.52
C ₂ H ₂	11.49*	11.52	11.59	11.53

TABLE I. Experimental vertical ionization potentials (IP, in eV), together with our QSGW results and independent QSGW reference values from two GW100 external datasets (ADF STO extra and TM def2-TZVPP). For *GW*-based methods, IPs correspond to $-\varepsilon_{\text{H}}^{\text{QP}}$, where $\varepsilon_{\text{H}}^{\text{QP}}$ is the converged HOMO quasiparticle energy. Experimental IPs are those compiled in Ref. [58] (Table 2 therein; values marked * are vertical, following that compilation). Each molecule employs the `really_tight` NAO basis tier and 32 frequency points. The external QSGW reference values are taken from the GW100 database [73] (see main text for details). Entries marked “—” indicate missing values.

tiers and have been shown to yield well-converged G^0W^0 quasiparticle gaps for NAO-based all-electron implementations on similar benchmark sets. We therefore adopt the same basis tiers for QSGW to provide a consistent and well-tested numerical baseline for the present benchmarks.

IV. BENCHMARK RESULTS

To comprehensively evaluate the accuracy and reliability of our NAO-based QSGW implementation, we perform systematic benchmark calculations on both molecular and periodic systems. For molecular systems, we select representative small molecules from the GW100 test set [58]. For periodic systems, we select a diverse range of materials, including typical semiconductors, wide-gap insulators, and rare gas solids, allowing us to assess the performance of our implementation across different bonding types and band gap ranges. In all cases, we compare our QSGW results with standard DFT functionals, one-shot G^0W^0 calculations, other QSGW implementations, and experimental values where available.

A. Molecular Benchmarks

To validate our QSGW implementation for molecular systems, we perform benchmark calculations on a selection of small molecules from the GW100 test set [58, 74–76].

As an initial validation of the present implementation, we consider a representative subset of small molecules from the GW100 test set (Table I). The selected molecules (Ag₂, AlF₃, As₂, AsH₃, BF, BH₃, and C₂H₂) cover diverse bonding characters and chemical environments, including a metallic dimer (Ag₂), an ionic fluoride (AlF₃), *p*-block elemental/covalent species (As₂, AsH₃), a polar diatomic (BF), an electron-deficient hydride (BH₃), and a small π -bonded hydrocarbon (C₂H₂).

Together, they provide a compact yet nontrivial validation set for the present implementation.

Table I presents the vertical ionization potentials (IPs) from this work and compares them with experimental reference values and QSGW benchmarks from established implementations (GW100 external datasets). In *GW*-based quasiparticle approaches, IPs correspond to $-\varepsilon_{\text{H}}^{\text{QP}}$, where $\varepsilon_{\text{H}}^{\text{QP}}$ is the converged HOMO quasiparticle energy.

Accordingly, we compare our QSGW ionization potentials against the experimental reference data reported in Ref. [58] and against available molecular QSGW benchmarks from established implementations as compiled in the GW100 database [73] (Table I).

In Table I, the GW100 reference datasets are labeled by the underlying code and basis setting. In particular, “ADF STO extra” refers to the QSGW HOMO dataset computed with the Amsterdam Density Functional (ADF) code using a Slater-type orbital (STO) basis in the larger “extra” basis sets [70] as provided in the GW100 database (GW100 file `qsGW_HOMO_ADF_STO_extra.json`). Likewise, “TM def2-TZVPP” refers to the QSGW HOMO dataset computed with TURBOMOLE (TM) using the Gaussian def2-TZVPP basis sets [75] as provided in the GW100 database (GW100 file `qsGW_HOMO_Tv6.0_def2-TZVPP.json`).

This code-to-code comparison provides an additional consistency check for our molecular QSGW implementation. As shown in Table I, our QSGW IPs agree well with reference QSGW values from other implementations (ADF STO extra and TM def2-TZVPP), with deviations within ~ 0.4 eV for this subset.

B. Semiconductors and Insulators

We now turn to periodic systems, where we present the QSGW results for a set of semiconductors and insulators calculated by LibRPA. The crystal structure prototypes used for the periodic benchmark set are summarized in Table II.

System	Prototype	a (Å)	c (Å)
Si	diamond	5.431	—
C	diamond	3.567	—
SiC	zinc blende	4.358	—
BN	zinc blende	3.616	—
BP	zinc blende	4.538	—
AIP	zinc blende	5.463	—
MgO	rock salt	4.211	—
wAlN	wurtzite	3.110	4.980
wZnO	wurtzite	3.250	5.207
GaAs	zinc blende	5.654	—
Ne	fcc	4.195	—

TABLE II. Crystal structure prototypes and lattice constants (in Å) used for the periodic benchmark set in Table III. For cubic systems, c is not applicable.

Table III presents the band gaps of a series of semiconductors and insulators computed by our NAO-based QSGW implementation. We first prioritize validation against established implementations by comparing our QSGW gaps to literature benchmarks from independent codes (Table III). In particular, we list QSGW reference values obtained with crystalline Gaussian basis sets [51] and all-electron LAPW-based QSGW benchmark values [49]. For additional context on the spread across widely used implementations, we also list representative self-consistent GW-family reference results obtained within a PMT (plane waves plus muffin-tin orbitals) hybrid-QSGW workflow [50], a PAW-based fully self-consistent GW implementation [77], and a plane-wave self-consistent GW scheme with efficient vertex corrections [78].

To facilitate cross-code validation, we treat the Gaussian-QSGW [51] and LAPW-QSGW [49] columns in Table III as our primary QSGW reference benchmarks where available. The remaining literature columns (PMT hQSGW [50], PAW scGW [77], and PW scGW+vertex [78]) represent closely related self-consistent GW-family workflows and are included to make the spread across widely used approaches explicit; since they are not strictly at the same approximation level as standard QSGW, we use them as context rather than as one-to-one QSGW benchmarks. The superscript zb denotes that the corresponding ZnO value was reported for the zinc-blende structure in Ref. [77] (as compiled in Ref. [51]).

As illustrated in Fig. 5, the PBE functional systematically underestimates the band gaps for this benchmark set. The single-shot G^0W^0 @PBE method captures most of the gap opening relative to PBE, while QSGW provides a further systematic correction on top of G^0W^0 @PBE under the present protocol. In what follows, we validate our QSGW gaps against independent QSGW benchmarks from the literature, and list experimental gaps only as context.

First, we assess cross-implementation consistency by comparing our QSGW gaps with literature QSGW benchmarks from independent implementations, focusing

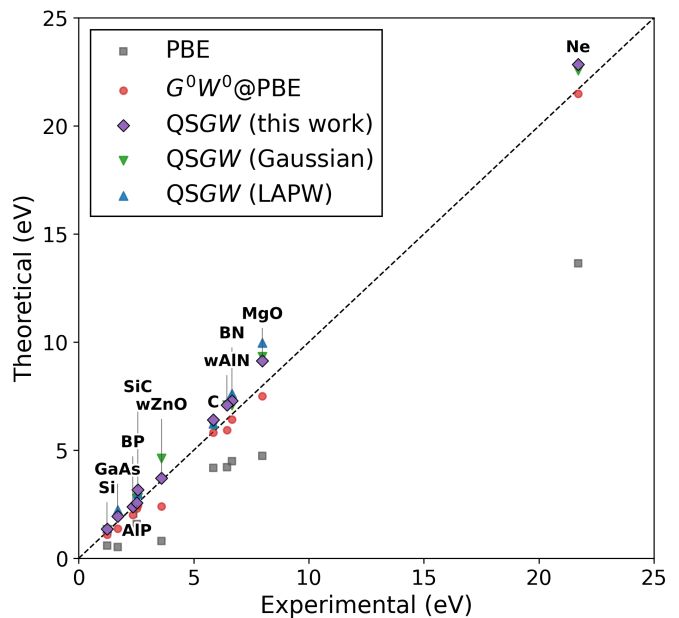


FIG. 5. Band gaps of semiconductors and insulators computed with PBE, G^0W^0 @PBE, and QSGW under the numerical atomic orbital (NAO) framework in LibRPA.

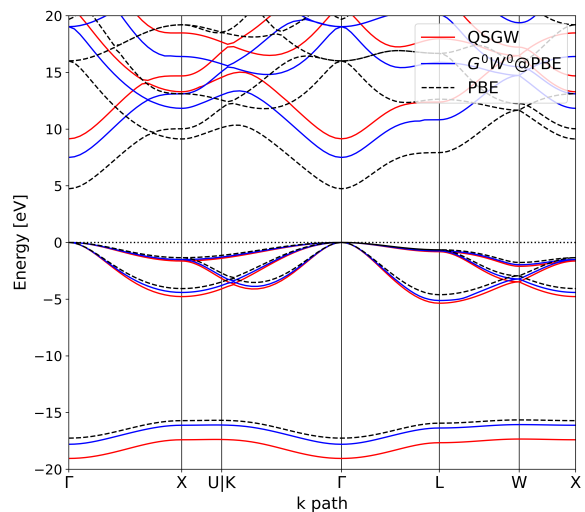


FIG. 6. Band structure of MgO calculated using PBE (FHI-aims) and QSGW (LibRPA). The calculations employed an $8 \times 8 \times 8$ k-point mesh, a frequency grid of 16 points, and the `intermediate_gw` basis sets.

on Gaussian-QSGW [51] and LAPW-QSGW [49] (Table III). We define $\Delta E_g \equiv E_g^{(\text{this work})} - E_g^{(\text{ref})}$ in eV and report it for each system in Table III. For the systems available in common, the deviations are typically within ~ 0.3 eV, with the largest discrepancies for wZnO ($\Delta E_g = -0.92$ eV relative to Gaussian-QSGW) and MgO ($\Delta E_g = -0.83$ eV relative to LAPW-QSGW). Overall, the cross-code deviations are comparable to the spread seen among published periodic QSGW benchmarks and

System	PBE	G^0W^0 @PBE	QSGW (this work)	Literature (independent implementations / reference workflows)						Expt.
				Gaussian QSGW [51]	LAPW QSGW [49]	PMT hQSGW [50]	PAW scGW [77]	PW scGW+vertex [78]	FP-LMTO QSGW [40]	
Si	0.59	1.09	1.36	1.32	1.39	1.28	1.49	1.47	1.25	1.23
C	4.18	5.82	6.41	6.14	6.23	6.11	6.43	6.40	5.97	5.85
SiC	1.38	2.46	3.17	2.81	3.00	2.63	2.88	2.90	2.53	2.57
BN	4.50	6.42	7.29	7.07	7.62	—	7.50	7.51	—	6.66
BP	1.25	2.01	2.39	—	—	—	—	—	—	2.35
AlP	1.58	2.30	2.56	2.76	—	2.74	2.94	3.10	—	2.53
MgO	4.74	7.50	9.14	9.33	9.97	8.97	9.58	9.29	—	7.98
wAlN	4.22	5.93	7.10	7.09	—	6.91	—	—	—	6.44
wZnO	0.81	2.40	3.71	4.63	—	3.88	4.29 ^{zb}	4.61	3.87	3.60
GaAs	0.53	1.37	1.94	—	2.24	—	—	—	1.74	1.69
Ne	13.64	21.49	22.84	22.57	—	—	—	—	—	21.7
MARE (%)	45.64	10.05	9.43	—	—	—	—	—	—	—
MPE (%)	-45.64	-10.05	+9.43	—	—	—	—	—	—	—

TABLE III. Band gaps (in eV) of semiconductors and insulators. An $8 \times 8 \times 8$ \mathbf{k} -point mesh was employed for most systems, with the exception of wAlN and wZnO ($8 \times 8 \times 5$). All calculations utilized a frequency grid of 16 points and the `intermediate_gw` basis sets (see Sec. III C 2). Experimental band gaps are taken from Ref. [60] (and references therein), except for Ne which is taken from Ref. [79]. For BP, reported experimental values vary (2.2–2.5 eV); we use the midpoint 2.35 eV when computing the error metrics. Literature reference values are cited in the column headers (see main text for interpretation details). The Mean Absolute Relative Error (MARE) and Mean Percentage Error (MPE) with respect to experimental values are listed at the bottom for PBE, G^0W^0 @PBE, and our QSGW results. The MPE indicates systematic underestimation (negative values) or overestimation (positive values). **All values are reported to two decimal places.**

support the validity of the present NAO-based QSGW workflow at the level of established implementations.

Similarly, for wide-gap insulators like C (diamond) and BN, our results (6.41 eV and 7.29 eV) are consistent with the literature benchmarks listed in Table III. This agreement suggests that our implementation, utilizing the space-time formalism and LRI technique within the NAO framework, captures the essential QSGW physics at a level comparable to established implementations used in published periodic benchmarks.

A notable deviation is observed for wurtzite ZnO (wZnO), a system known to be challenging for GW methods. Our calculated QSGW band gap is 3.71 eV, which is lower than several established cross-code reference values reported for ZnO in the literature (Table III). wZnO is notoriously difficult to converge in GW calculations due to the strong hybridization between Zn $3d$ states and O $2p$ states, as well as the slow convergence with respect to high-energy unoccupied states.

Interestingly, while G^0W^0 @PBE shows a large underestimation for wZnO (33.3% error), our QSGW result overestimates by only 3.1%, indicating that quasiparticle self-consistency improves the gap relative to G^0W^0 @PBE for this material within the present numerical protocol. Previous studies have shown that, in the LAPW framework, adding high-energy local orbitals (HLOs) can significantly increase the GW band gap of ZnO [80]. The underestimation of the G^0W^0 band gap for ZnO within the standard NAO basis sets has been discussed in Ref. [72]. It has been shown [72] that the issue can be mitigated by complementing NAOs with highly localized Slater-type orbitals (STOs), in analogy with the LAPW+HLOs scenario.

For the rare gas solid Ne, our QSGW result (22.84 eV) is in excellent agreement with the periodic QSGW benchmark value (22.57 eV) reported in Ref. [51] and with the

experimental value (21.7 eV). This confirms that our implementation reliably describes wide-gap systems with diverse bonding characteristics, from covalent semiconductors to weakly interacting rare gas solids.

To further illustrate the quality of our QSGW calculations beyond band gap values, we present the full band structure of MgO in Fig. 6. From PBE to G^0W^0 @PBE, there is a significant increase in the band gap while preserving the overall shape of the band dispersion. From G^0W^0 @PBE to QSGW, the band gap is further opened up, as expected. The smooth and continuous bands across the Brillouin zone indicate the numerical stability of our implementation under the protocol described in Secs. III A–III C.

We further observe that the bands immediately below the valence-band maximum are very similar between QSGW and G^0W^0 @PBE, whereas deeper valence bands in the energy region around -17 eV are shifted to lower energies in QSGW (Fig. 6). This non-rigid re-alignment reflects the state- and energy-dependent nature of the GW self-energy and the accompanying changes in screening along the self-consistent cycle, as also discussed in the literature [40, 49]. We expect that the energy positions of these deeper valence states are better described in QSGW.

In summary, benchmark calculations demonstrate that our all-electron QSGW implementation in LibRPA is reliable and accurate. It exhibits the typical systematic overestimation of band gaps characteristic of the QSGW approximation, consistent with other state-of-the-art implementations. The combination of NAOs, LRI, and the space-time formalism provides a practical all-electron framework for QSGW calculations for both molecules and periodic solids within LibRPA.

V. CONCLUSION AND OUTLOOK

We have developed and validated an all-electron implementation of the QSGW method for molecules and periodic systems within the numerical atomic orbital (NAO) framework of LibRPA, based on the space-time formalism and the localized resolution of identity (LRI) technique.

We analyzed numerical aspects specific to QSGW in this framework, in particular, the stability of the Padé analytic continuation and its basis representation dependence, and identified “Mode B” as the more robust construction within our current protocol. Benchmark calculations for a set of small molecules and for representative semiconductors and insulators show that the resulting IPs and quasiparticle gaps are consistent with established reference implementations, providing strong validation of the correctness of our implementation. For the crystalline solids, we obtain an MARE of 9.43% (MPE of +9.43%) relative to experiment, while for the molecular subset in Table I, we obtain an MARE of 3.64% (MPE of +2.12%) for the vertical ionization potentials relative to experiment.

Consistent with the known behavior of standard QSGW, the gaps are systematically overestimated, reflecting under-screening of the Coulomb interaction in the absence of vertex corrections [39, 81].

Looking forward, the present NAO-based QSGW

framework provides a practical starting point for incorporating vertex corrections in W and/or Σ [37, 42, 43, 46] and for combining QSGW with dynamical mean-field theory for strongly correlated materials [82–87]. On the numerical side, more robust analytic continuation schemes and further basis-set optimization will be important to reduce residual instabilities in challenging cases. In particular, addressing basis-set completeness for ionic oxides (e.g., ZnO) via targeted basis augmentation and systematic extrapolation is an important next step. Finally, the availability of a quasiparticle Hamiltonian enables extensions to neutral excitations via QSGW–BSE [88] and to other applications such as core-level binding energies [89], relativistic two-component GW [90], magnetic systems [91], and data-driven modeling [92]. Going beyond the GW approximation to include higher-order correlations [93] remains an active research direction.

ACKNOWLEDGMENTS

We acknowledge the funding support from the National Key Research and Development Program of China (Grant Nos. 2023YFA1507004 and 2022YFA1403800) and the Strategic Priority Research Program of the Chinese Academy of Sciences under Grant No. XDB0500201. This work was also supported by the National Natural Science Foundation of China (Grants Nos. 12134012, 12374067, and 12188101).

-
- [1] P. Hohenberg and W. Kohn, *Physical Review* **136**, B864 (1964).
- [2] W. Kohn and L. J. Sham, *Physical Review* **140**, A1133 (1965).
- [3] L. Hedin, *Physical Review* **139**, A796 (1965).
- [4] G. Strinati, H. J. Mattausch, and W. Hanke, *Physical Review B* **25**, 2867 (1982).
- [5] M. S. Hybertsen and S. G. Louie, *Physical Review B* **35**, 5585 (1987).
- [6] R. W. Godby, M. Schlüter, and L. J. Sham, *Physical Review B* **37**, 10159 (1988).
- [7] F. Aryasetiawan and O. Gunnarsson, *Physical Review Letters* **74** (1995), 10.1103/physrevlett.74.3221.
- [8] W. G. Aulbur, L. Jönsson, and J. W. Wilkins, in *Solid State Physics*, Vol. 54 (Elsevier, 2000) pp. 1–218.
- [9] G. Onida, L. Reining, and A. Rubio, *Reviews of Modern Physics* **74**, 601 (2002).
- [10] P. Rinke, A. Qteish, J. Neugebauer, C. Freysoldt, and M. Scheffler, *New Journal of Physics* **7**, 126 (2005).
- [11] N. Marom, F. Caruso, X. Ren, O. T. Hofmann, T. Körzdörfer, J. R. Chelikowsky, A. Rubio, M. Scheffler, and P. Rinke, *Physical Review B* **86**, 245127 (2012).
- [12] D. Golze, M. Dvorak, and P. Rinke, *Frontiers in Chemistry* **7** (2019), 10.3389/fchem.2019.00377.
- [13] L. Reining, *WIREs Comput. Mol. Sci.* **8**, e1344 (2018).
- [14] M. F. Lange and T. C. Berkelbach, *J. Chem. Theory Comput.* **14**, 4224 (2018).
- [15] J. P. Perdew, K. Burke, and M. Ernzerhof, *Physical Review Letters* **77**, 3865 (1996).
- [16] F. Bruneval and M. A. L. Marques, *J. Chem. Theory Comput.* **9**, 324 (2013).
- [17] T. Körzdörfer and N. Marom, *Physical Review B* **86**, 041110 (2012).
- [18] W. Chen and A. Pasquarello, *Physical Review B* **90**, 165133 (2014).
- [19] S. E. Gant, J. B. Haber, M. R. Filip, F. Sagredo, D. Wing, G. Ohad, L. Kronik, and J. B. Neaton, *Phys. Rev. Mater.* **6**, 053802 (2022).
- [20] L. Zhang, Y. Shu, C. Xing, X. Chen, S. Sun, Y. Huang, and D. G. Truhlar, *Journal of Chemical Theory and Computation* **18**, 3523 (2022).
- [21] W. Ku and A. G. Eguiluz, *Physical Review Letters* **89** (2002), 10.1103/physrevlett.89.126401.
- [22] A. Stan, N. E. Dahlen, and R. van Leeuwen, *Europhysics Letters (EPL)* **76**, 298 (2006).
- [23] C. Rostgaard, K. W. Jacobsen, and K. S. Thygesen, *Phys. Rev. B* **81** (2010), 10.1103/physrevb.81.085103.
- [24] F. Caruso, P. Rinke, X. Ren, A. Rubio, and M. Scheffler, *Physical Review B* **88**, 075105 (2013).
- [25] F. Caruso, P. Rinke, X. Ren, M. Scheffler, and A. Rubio, *Phys. Rev. B* **86**, 081102(R) (2012).
- [26] A. L. Kutepov, *Phys. Rev. B* **94**, 155101 (2016).
- [27] A. L. Kutepov, *Phys. Rev. B* **95**, 195120 (2017).
- [28] M. Shishkin and G. Kresse, *Phys. Rev. B* **75**, 235102 (2007).
- [29] M. Grumet, P. Liu, M. Kaltak, J. Klimeš, and G. Kresse,

- Phys. Rev. B **98**, 155143 (2018).
- [30] B. Holm and U. von Barth, *Physical Review B* **57**, 2108 (1998).
- [31] P. Koval, D. Foerster, and D. Sánchez-Portal, *Physical Review B* **89**, 155417 (2014).
- [32] M. Wen, V. Abraham, G. Harsha, A. Shee, K. B. Whaley, and D. Zgid, *Journal of Chemical Theory and Computation* **20**, 3109 (2024).
- [33] E. Maggio and G. Kresse, *Journal of chemical theory and computation* **13**, 4765 (2017).
- [34] A. L. Kutepov, S. Y. Savrasov, and G. Kotliar, *Phys. Rev. B* **80**, 041103 (2009).
- [35] G. Baym and L. P. Kadanoff, *Physical Review* **124**, 287 (1961).
- [36] G. Baym, *Physical Review* **127**, 1391 (1962).
- [37] M. Shishkin, M. Marsman, and G. Kresse, *Physical review letters* **99**, 246403 (2007).
- [38] S. V. Faleev, M. van Schilfhaarde, and T. Kotani, *Phys. Rev. Lett.* **93**, 126406 (2004).
- [39] M. van Schilfhaarde, T. Kotani, and S. Faleev, *Physical Review Letters* **96**, 226402 (2006).
- [40] T. Kotani, M. Van Schilfhaarde, and S. V. Faleev, *Physical Review B* **76**, 165106 (2007).
- [41] A. Marie and P.-F. c. Loos, *Journal of Chemical Theory and Computation* **19**, 3943 (2023).
- [42] B. Cunningham, M. Grüning, D. Pashov, and M. van Schilfhaarde, *Phys. Rev. B* **108**, 165104 (2023).
- [43] A. L. Kutepov, *Phys. Rev. B* **105**, 045124 (2022).
- [44] A. Förster, *J. Chem. Theory Comput.* **21**, 767 (2025).
- [45] H. Sakakibara, T. Kotani, M. Obata, and T. Oda, *Physical Review B* **101**, 205120 (2020).
- [46] A. Förster and L. Visscher, *Physical Review B* **105**, 125121 (2022).
- [47] W. R. Lambrecht, C. Bhandari, and M. Van Schilfhaarde, *Physical Review Materials* **1**, 043802 (2017).
- [48] S. Das, J. E. Coulter, and E. Manousakis, *Physical Review B* **91**, 115105 (2015).
- [49] N. Salas-Illanes, D. Nabok, and C. Draxl, *Physical Review B* **106**, 045143 (2022).
- [50] D. Deguchi, K. Sato, H. Kino, and T. Kotani, *Japanese Journal of Applied Physics* **55**, 051201 (2016).
- [51] J. Lei and T. Zhu, *The Journal of Chemical Physics* **157**, 214114 (2022).
- [52] M. Obata, T. Kotani, and T. Oda, *Computational Materials Science* **260**, 114190 (2025).
- [53] M. Shishkin and G. Kresse, *Phys. Rev. B* **74**, 035101 (2006).
- [54] M. Feyereisen, G. Fitzgerald, and A. Komornicki, *Chemical physics letters* **208**, 359 (1993).
- [55] O. Vahtras, J. Almlöf, and M. Feyereisen, *Chemical Physics Letters* **213**, 514 (1993).
- [56] F. Weigend, M. Häser, H. Patzelt, and R. Ahlrichs, *Chemical physics letters* **294**, 143 (1998).
- [57] A. Förster and L. Visscher, *J. Chem. Theory Comput.* **16**, 7381 (2020).
- [58] M. J. van Setten, F. Caruso, S. Sharifzadeh, X. Ren, M. Scheffler, F. Liu, J. Lischner, L. Lin, J. R. Deslippe, and S. G. Louie, *J. Chem. Theory Comput.* **11**, 5665 (2015).
- [59] X. Ren, P. Rinke, V. Blum, J. Wieferink, A. Tkatchenko, A. Sanfilippo, K. Reuter, and M. Scheffler, *New Journal of Physics* **14**, 053020 (2012).
- [60] X. Ren, F. Merz, H. Jiang, Y. Yao, M. Rampp, H. Lederer, V. Blum, and M. Scheffler, *Physical Review Materials* **5**, 013807 (2021).
- [61] M.-Y. Zhang, P. Lin, R. Shi, M. Scheffler, and X. Ren, “Low-scaling *gw* calculation of quasi-particle energies within numerical atomic orbital framework,” (2026), arXiv preprint, in preparation.
- [62] S. Ismail-Beigi, *Journal of Physics: Condensed Matter* **29**, 385501 (2017).
- [63] R. Shi, M.-Y. Zhang, P. Lin, L. He, and X. Ren, *Computer Physics Communications* **309**, 109496 (2025).
- [64] P. Lin, X. Ren, and L. He, *The Journal of Physical Chemistry Letters* **11**, 3082 (2020).
- [65] R. Shi, P. Lin, M.-Y. Zhang, L. He, and X. Ren, *Physical Review B* **109**, 035103 (2024).
- [66] M. Kaltak, J. Klimeš, and G. Kresse, *Journal of Chemical Theory and Computation* **10**, 2498 (2014).
- [67] S. Azizi, M. Kaltak, J. Klimeš, and G. Kresse, *Journal of Open Source Software* **8**, 5160 (2023).
- [68] H. Vidberg and J. Serene, *Journal of Low Temperature Physics* **29**, 179 (1977).
- [69] P. Pulay, *Chemical Physics Letters* **73**, 393 (1980).
- [70] A. Förster and L. Visscher, *Frontiers in Chemistry* **9**, 736591 (2021).
- [71] FHI-aims team, *FHI-aims: All-Electron Electronic Structure Theory with Numeric Atom-Centered Basis Functions – A Users’ Guide* (2025), version 250822.1. See also manual section “Defaults for chemical elements: species_defaults” (Sec. 2.2).
- [72] X. Ren, F. Merz, H. Jiang, Y. Yao, M. Rampp, H. Lederer, V. Blum, and M. Scheffler, *Phys. Rev. Materials* **5**, 013807 (2021), arXiv:2011.01400 [cond-mat.mtrl-sci].
- [73] “Gw100 benchmark set: Data repository,” <https://github.com/setten/GW100> (2026), accessed 2026-02-22. Repository contains curated benchmark datasets (including qsGW HOMO/LUMO JSON files) associated with published GW100/q sGW benchmark studies (e.g., DOI: 10.1021/acs.jctc.6b00774; DOI: 10.3389/fchem.2021.736591).
- [74] F. Kaplan, M. E. Harding, C. Seiler, F. Weigend, F. Evers, and M. J. van Setten, *J. Chem. Theory Comput.* **12**, 2528 (2016).
- [75] F. Caruso, M. Dauth, M. J. van Setten, and P. Rinke, *J. Chem. Theory Comput.* **12**, 5076 (2016).
- [76] M. J. van Setten, F. Weigend, and F. Evers, *J. Chem. Theory Comput.* **9**, 232 (2013).
- [77] M. Grumet, P. Liu, M. Kaltak, J. Klimeš, and G. Kresse, *Physical Review B* **98**, 155143 (2018).
- [78] W. Chen and A. Pasquarello, *Physical Review B* **92**, 041115 (2015).
- [79] N. Schwentner, F.-J. Himpsel, V. Saile, M. Skibowski, W. Steinmann, and E. Koch, *Physical Review Letters* **34**, 528 (1975).
- [80] H. Jiang and P. Blaha, *Physical Review B* **93**, 115203 (2016).
- [81] F. Bruneval and M. Gatti, *Top. Curr. Chem.* **347**, 99 (2014).
- [82] S. Biermann, F. Aryasetiawan, and A. Georges, *Phys. Rev. Lett.* **90**, 086402 (2003).
- [83] G. Kotliar, S. Y. Savrasov, K. Haule, V. S. Oudovenko, O. Parcollet, and C. A. Marianetti, *Rev. Mod. Phys.* **78**, 865 (2006).
- [84] S. Choi, A. Kutepov, K. Haule, M. van Schilfhaarde, and G. Kotliar, *npj Quantum Mater.* **1**, 16001 (2016).
- [85] T. Zhu and G. K.-L. Chan, *Physical Review X* **11**, 021006 (2021).

- [86] J. Lee and K. Haule, *Phys. Rev. B* **95**, 155104 (2017).
- [87] F. Nilsson, L. Boehnke, P. Werner, and F. Aryasetiawan, *Phys. Rev. Materials* **1**, 043803 (2017).
- [88] A. Förster and L. Visscher, *Journal of Chemical Theory and Computation* **18**, 6779 (2022).
- [89] J. Li, Y. Jin, P. Rinke, W. Yang, and D. Golze, *J. Chem. Theory Comput.* **18**, 7570 (2022).
- [90] A. Förster, E. van Lenthe, E. Spadetto, and L. Visscher, *J. Chem. Theory Comput.* **19**, 5958 (2023).
- [91] P. Pokhilko and D. Zgid, *J. Chem. Phys.* **157**, 144101 (2022).
- [92] S. Takano, T. Kotani, M. Obata, K. Sato, H. Saito, H. Fujii, and T. Oda, *Japanese Journal of Applied Physics* (2025), 10.35848/1347-4065/ae3bc0.
- [93] B. Cunningham, *Phys. Rev. Research* **6**, 043277 (2024).